Nuclear collective motion of heavy nuclei with axial quadrupole and octupole deformation

R. Budaca,[1,2,*] P. Buganu,[1] and A. I. Budaca[1]

[1] *"Horia Hulubei" National Institute for Physics and Nuclear Engineering, Str. Reactorului 30, RO-077125, POB-MG6 Bucharest-Măgurele, Romania*

[2] *Academy of Romanian Scientists, Splaiul Independenţei 54, 050044, Bucharest, Romania*

(Received 8 June 2022; accepted 6 July 2022; published 18 July 2022)

A quadrupole-octupole axially symmetric model is constructed for the unified description of alternate parity bands corresponding to octupole vibration or a stable deformation. The model depends on two parameters whose clear physical meaning allows a systematic description of the rotation-vibration dynamics of alternate parity bands analyzed for isotopic sequences of Ra, Th, U, and Pu nuclei. A critical point is identified in the $A =$ 224–228 mass region of the Ra and Th nuclei marking different stages of the transition between static and dynamic octupole deformation. Model predictions are performed for energies of unobserved states of the yrast sequence and of the excited bands as well as for the $E1$, $E2$, and $E3$ transition rates, which reproduce the available experimental data and exhibit a specific spin dependence for the transitional nuclei.

DOI: 10.1103/PhysRevC.106.014311

I. INTRODUCTION

Atomic nuclei are predominantly axially symmetric in their ground state [1]. Most notable exceptions from axial symmetry include triaxial and reflection asymmetric (pear-like) shapes. The reflection asymmetric nuclei imply a sizable odd multipolarity component of the deformation. The most important one is the octupole deformation, whose microscopic origin is the strong coupling between single-particle states, which differ in orbital and total angular momentum by $\Delta l, \Delta j = 3$. The restoration of reflection symmetry generates two rotational bands of opposite parity with equal angular momentum projection K on the symmetry axis. The observation of a negative-parity band with levels $L^\pi = 1^-, 3^-, 5^-, \ldots$, lying close to the ground-state band, is thus considered as a clear signature of octupole deformation in even-even nuclei. Such doubled bands are notably reported in light rare earth and actinide nuclei [2–4]. If the intrinsic states with opposite values of octupole deformation are isolated from each other, then the observed bands are simply constructed on symmetric and antisymmetric superpositions of them. This is the case of static octupole deformation, where the two opposite parity bands merge into a single regular rotational band with alternating parity [5]. More often, the two intrinsic states interact, such that the restoration of the reflection symmetry in the laboratory frame is realized by the quantum tunneling between the intrinsic states. From the quantum mechanics point of view, the negative parity state will always be higher in energy, such that their experimental observation is an indication of the so-called octupole vibration [6].

In general, octupole degrees of freedom are superposed with the quadrupole ones. The problem of quadrupole-octupole collectivity is not easy to treat, neither microscopically, because of the breaking of reflection symmetry, nor geometrically, due to the difficulty in determining the total inertia tensor of the system. However, by preserving the axial symmetry or by considering an adiabatic decoupling of the degrees of freedom, the description of reflection asymmetric shapes is possible within a variety of microscopic, geometric, and algebraic approaches [7,8]. The nuclear shape can be ascertained from any mean field [9,10] or a microscopic-macroscopic approach [11], by the deformation parameters of the energy surface minimum. Nevertheless, the microscopic description of alternate parity bands is usually based on a mean field with a static octupole deformation or very stabilized equilibrium shape fluctuations, combined with beyond mean-field approaches such as random phase approximation, generator coordinate model, or interacting boson model mappings [3,7,8]. An alternative description of alternate parity bands comes from the assumption that the reflection asymmetric shape is a consequence of clustering. An example of such an approach is the *spdf* extension of the interacting boson model [12,13], where the standard quadrupole bosons s and d, are complemented by the odd parity octupole boson f and the dipole boson s, the later being essential for the description of cluster configurations. The same phenomenology was used in the conception of the binary cluster model, which uses a radial equation for the description of alternate parity bands [14], whose variable is related to the distance between clusters with an *a priori* fixed mass asymmetry. This template was also used to define a cluster model with a variable associated instead with the mass asymmetry [15]. All these approaches use clustering for the explanation of the emerging negative parity bands, disregarding to some extent the actual deformation of the nucleus.

The Bohr geometrical approach is one of the few models which deals with the interplay between the octupole and

*Corresponding author: rbudaca@theory.nipne.ro

quadrupole degrees of freedom [1]. The usually complex quadrupole-octupole Bohr Hamiltonian [16] is significantly simplified within axial symmetry [17–20], and can be even exactly separated between the rotation degrees of freedom, a generalized deformation coordinate, and an angular variable responsible for the coherent superposition of the octupole and quadrupole deformations. The method is valid even for higher order multipolarity and can be analytically solved in certain conditions [21,22], leading even to a parameter free model [23]. The parity splitting mechanism is contained in the angular variable potential having two symmetrical minima. The associated problem is usually approximated with symmetric harmonic oscillators with [18,19,24], or without [22,23,25] a constant energy shift which is empirically introduced to account for the tunneling between the two potential minima. The tunneling mechanism is rarely treated consistently, being considered usually for adiabatically decoupled octupole deformation [20,21] or simulated within an alternative parity splitting scenario [26]. We propose in this study to treat exactly the angular equation corresponding to the relative quadrupole-octupole interplay. This is achieved with a suitably chosen analytical form of the double well potential evolving with increasing spin from a single minimum to a double minimum structure with an increasing barrier height and width and more separated minima. The lowest energies will then incorporate a spin-dependent parity splitting contribution emerging solely due to the geometry of the quadrupole-octupole coupling. The program is aimed for the description of yrast alternate parity bands in Ra and light actinide nuclei.

II. THEORETICAL FORMALISM

A. Hamiltonian and separation of variables

For quadrupole (β_2) and octupole (β_3) deformation variables constrained to axial symmetry, the overly complex general Bohr Hamiltonian [1] reduces to [18,19]

$$H = -\sum_{\lambda=2,3} \frac{\hbar^2}{2B_\lambda} \frac{1}{\beta_\lambda^3} \frac{\partial}{\partial \beta_\lambda} \beta_\lambda^3 \frac{\partial}{\partial \beta_\lambda} + \frac{\hbar^2 \hat{L}^2}{6\left(B_2\beta_2^2 + 2B_3\beta_3^2\right)} + U(\beta_2, \beta_3), \quad (2.1)$$

where B_2 and B_3 are the corresponding mass parameters. The solutions of the above Hamiltonian are of the form

$$\Phi^{\pm}_{LMK}(\beta_2, \beta_3, \theta) = (\beta_2\beta_3)^{-3/2} \Psi^{\pm}_L(\beta_2, \beta_3) |LMK, \pm\rangle. \quad (2.2)$$

M and K are the eigenvalues of the angular momentum projection operators on the z axis of the laboratory and intrinsic reference frames related through the Euler angles θ. The $\pm$ assignment of the rotation function [18,19,22,25] refers to its symmetry or antisymmetry with respect to reflection in the plane perpendicular to the intrinsic symmetry axis. In what follows, we concern ourselves only with the $K = 0$ case.

With the notations

$$\tilde{\beta}_2 = \beta_2\sqrt{\frac{B_2}{B}}, \quad \tilde{\beta}_3 = \beta_3\sqrt{\frac{B_3}{B}}, \quad B = \frac{B_2 + B_3}{2},$$

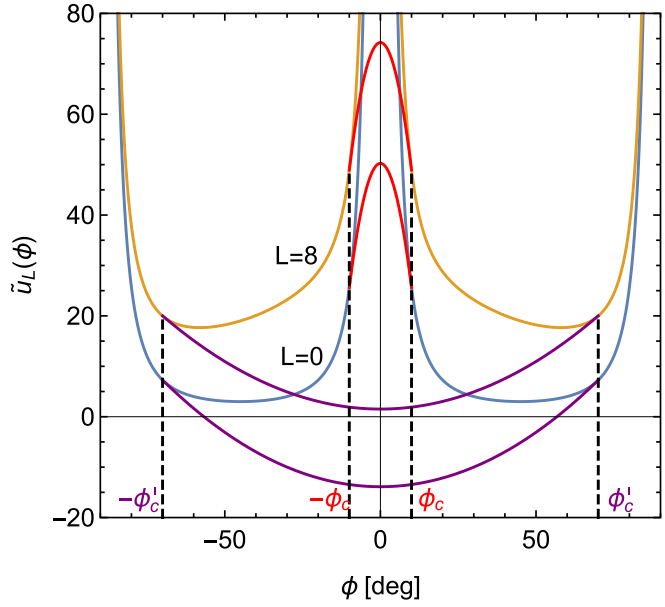

FIG. 1. The original potential $u_L(\phi)$ Eq. (2.8) for $L = 0$ and $L = 8$ with an infinite barrier at $\phi \to 0$ is presented along with its modified inner part $v(\phi)$ Eq. (2.9), represented by an inverted (red curve) and a normal parabola (purple curve) when $|\phi_c| = 10^\circ$ and, respectively, $|\phi_c'| = 70^\circ$. The corresponding conjunction points of the exact and modified potential regions are marked by horizontal dashed lines.

$$\epsilon = \frac{2B}{\hbar^2}E, \quad u = \frac{2B}{\hbar^2}U, \quad (2.3)$$

and the change to polar coordinates

$$\tilde{\beta}_2 = \tilde{\beta}\cos\phi, \quad \tilde{\beta}_3 = \tilde{\beta}\sin\phi, \quad \tilde{\beta} = \sqrt{\tilde{\beta}_2^2 + \tilde{\beta}_3^2}, \quad (2.4)$$

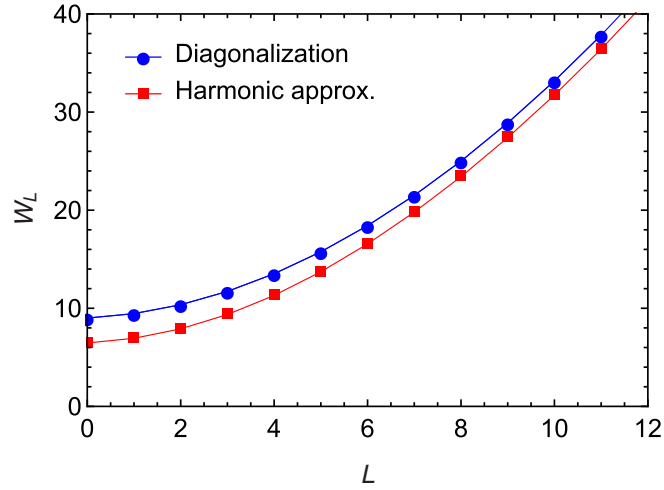

FIG. 2. Comparison between the harmonic approximation [23] and the diagonalization results for W_L when the barrier is infinite.

TABLE I. Parameters resulted from the fitting procedure with the best model are listed along with the resulted σ value, the excitation energy of the experimental 2^+ state, the last positive parity $L^+_{\max}$ and negative parity $L^-_{\max}$ experimental states considered in the fit as well as the critical angular momentum L^p_c marking the emergence of double minima in the $\tilde{u}_L(\phi)$ potential. The $(*)$ denotes experimental bands with missing low-lying states, see Figs. 5 and 7.

Nucl.	$L^+_{\max}/L^-_{\max}$	pot.	$\lvert\phi_c\rvert$	L^p_c	w_0	σ	$E_{\exp}(2^+)$ [keV]
^{224}Ra	$24^+/23^-$	ISW	30°	0^+	−1.491	0.188	84.37
^{226}Ra	$24^+/23^-$	ISW	54°	1^-	2.137	0.187	67.67
^{228}Ra	$22^+/19^-$	HO	69°	22^+	34.468	0.572	63.82
^{224}Th	$18^+/17^-$	ISW	29°	0^+	−2.851	0.223	98.10
^{226}Th	$20^+/19^-$	ISW	45°	6^+	4.147	0.169	72.20
^{228}Th	$22^+/19^-$	ISW	65°	15^-	10.129	0.375	57.77
^{230}Th	$24^+/21^-$	HO	72.6°	$>24^+$	68.702	0.747	53.20
^{232}Th	$24^+/23^-$	HO	78.2°	$>24^+$	141.177	0.519	49.37
^{234}Th	$24^+/23^{-*}$	HO	75.9°	$>24^+$	111.429	0.556	49.55
^{230}U	$22^+/17^-$	HO	70.2°	24^+	64.324	0.292	51.73
^{232}U	$24^+/21^-$	HO	76.8°	$>24^+$	123.407	0.203	47.60
^{234}U	$24^+/11^-$	HO	80.5°	$>24^+$	260.121	0.189	43.50
^{236}U	$24^+/19^-$	HO	78.6°	$>24^+$	179.246	0.358	45.24
^{238}U	$24^+/23^-$	HO	77.9°	$>24^+$	155.626	0.764	44.92
^{240}U	$24^+/21^{-*}$	HO	79.1°	$>24^+$	198.176	0.814	45.00
^{236}Pu	$16^+/5^-$	HO	79.3°	$>24^+$	210.496	0.064	44.63
^{238}Pu	$24^+/23^-$	HO	76.7°	$>24^+$	165.180	0.897	44.07
^{240}Pu	$24^+/23^-$	HO	76.5°	$>24^+$	148.866	1.068	42.82

Eq. (2.1) can be written, after integration on the Euler angles, as

$$\left[-\frac{\partial^2}{\partial\tilde{\beta}^2}-\frac{1}{\tilde{\beta}}\frac{\partial}{\partial\tilde{\beta}}+\frac{L(L+1)}{3\tilde{\beta}^2(1+\sin^2\phi)}-\frac{1}{\tilde{\beta}^2}\frac{\partial^2}{\partial\phi^2}+u(\tilde{\beta},\phi)+\frac{3}{\tilde{\beta}^2\sin^2 2\phi}-\epsilon_L\right]\Psi^{\pm}_L(\tilde{\beta},\phi)=0. \quad (2.5)$$

The newly introduced $\tilde{\beta}>0$ variable plays the role of a generalized deformation, while the angle $-\pi/2<\phi<\pi/2$ mediates the measure of interplay between quadrupole and octupole deformations. For example, one has pure quadrupole deformation for $\phi=0$, and pure octupole deformation $\pm\beta_3$ for $\phi=\pm\pi/2$ [18,19,22,25]. The above equation can be exactly separated if one considers a potential of the form $u(\tilde{\beta},\phi)=u(\tilde{\beta})+u(\phi)/\tilde{\beta}^2$ and a factorized total wave function $\Psi^{\pm}_L(\tilde{\beta},\phi)=\psi^{\pm}_L(\tilde{\beta})\chi^{\pm}_L(\phi)$. The radial-like equation is then defined as

$$\left[-\frac{\partial^2}{\partial\tilde{\beta}^2}-\frac{1}{\tilde{\beta}}\frac{\partial}{\partial\tilde{\beta}}+\frac{W^{\pm}_L}{\tilde{\beta}^2}+u(\tilde{\beta})\right]\psi^{\pm}_L(\tilde{\beta})=\epsilon_L\psi^{\pm}_L(\tilde{\beta}), \quad (2.6)$$

whereas the equation for the angular variable reads

$$\left[-\frac{\partial^2}{\partial\phi^2}+u(\phi)+u_L(\phi)\right]\chi^{\pm}_L(\phi)=W^{\pm}_L\chi^{\pm}_L(\phi) \quad (2.7)$$

with

$$u_L(\phi)=\frac{3}{\sin^2 2\phi}+\frac{L(L+1)}{3(1+\sin^2\phi)}. \quad (2.8)$$

B. The ϕ equation

Let us ignore at this step the additional potential $u(\phi)$, and concentrate on Eq. (2.7) for the potential (2.8), which emerges uniquely from the geometry of the axial quadrupole-octupole deformation space. The $u_L(\phi)$ potential is depicted in Fig. 1. It has a symmetric double well shape with an infinite separating barrier. The solutions in each well are equal and their symmetric and antisymmetric combination defines the wave function $\chi^{\pm}_L$. In order to determine these solutions, we diagonalized Eq. (2.7) in a basis of particle in the box states, only for the positive ϕ well. The obtained lowest states for each angular momentum are given in Fig. 2, where we also compared them with the harmonic approximation calculations made in Ref. [23]. As can be seen from Fig. 1, the potential is quite flat for lower angular momentum values, hence the larger departure of the harmonic approximation in respect to the diagonalization results. Nevertheless, with a suitable constant shift in energy which can be accommodated by the additional potential $u(\phi)$, the two evaluations have a rather compatible dependence on angular momentum.

Note that due to the infinite potential barrier, the odd-even L staggering (parity splitting) of energy levels is missing. In the framework of the present model, the tunneling effect is usually postulated by a constant contribution to the doubly degenerated energy state in either of the potential minima [19,24]. Here, we chose to approximate the inner part of the $u_L(\phi)$ with a finite barrier. In this way, one will be able to keep the maximum information coming from the geometry of the deformation space but also allow a controlled tunneling effect between the $\pm\phi$ potential minima. After few tries, we arrived at the conclusion that an inverted parabola is a sensible choice:

$$v(\phi)=-a\phi^2+b. \quad (2.9)$$

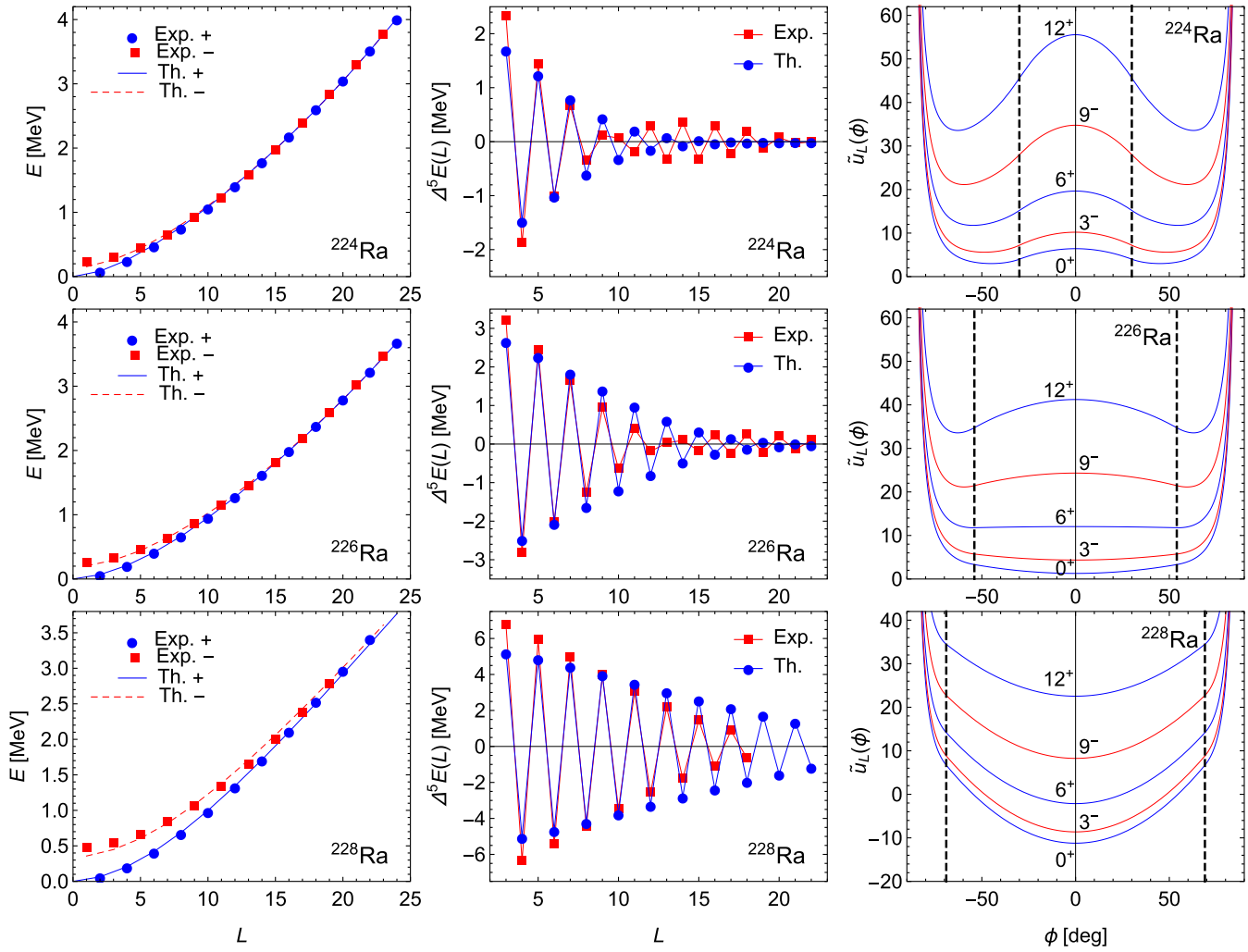

FIG. 3. Comparison between theoretical and experimental absolute energies (column 1) and $\Delta L = 1$ staggering measure (column 2) for ^{224}Ra [42], ^{226}Ra [44], and ^{228}Ra [46] nuclei. The last column depicts the evolution of the corresponding $\tilde{u}_L(\phi)$ potential for few selected angular momentum values with the dashed horizontal lines noting the matching points $\pm\phi_c$.

The parameters a and b are determined by demanding the satisfaction of continuity conditions at the conjunction point

$$u_L(\phi_c) = v(\phi_c), \quad \left.\frac{\partial u_L(\phi)}{\partial \phi}\right|_{\phi_c} = \left.\frac{\partial v(\phi)}{\partial \phi}\right|_{\phi_c}, \tag{2.10}$$

for a fixed value of the matching point $|\phi_c|$. It is easy to see that both parameters depend linearly on $L(L+1)$, and consequently $v(\phi)$ too, keeping thus the original dependence on L from $u_L(\phi)$. This also produces a tunneling or a vibrational effect which depends now on angular momentum. The modified potential is then defined as

$$\tilde{u}_L(\phi) = \begin{cases} v_L(\phi), & |\phi| < \phi_c \\ u_L(\phi), & |\phi| \geqslant \phi_c \end{cases} \tag{2.11}$$

with the matching procedure schematically exemplified in Fig. 1. It must be mentioned that the additional potential $u(\phi)$ ignored up to this point can be chosen in such a way as to be compatible with the adopted approximation. For the sake of generality, one will consider a constant contribution w_0 from $u(\phi)$. The associated differential equation in variable ϕ is then diagonalized in the same particle in the box wave functions which are now discriminated by the parity

$$f_n^+(\phi) = \sqrt{\frac{2}{\pi}} \cos(2n-1)\phi, \tag{2.12}$$

$$f_n^-(\phi) = \sqrt{\frac{2}{\pi}} \sin 2n\phi. \tag{2.13}$$

The symmetric $(+)$ basis is used for even L positive parity states, and, respectively, odd L negative parity states are associated with antisymmetric $(-)$ basis solutions. The final solution of the equation for the angular variable is expressed as $\chi_s^{\pm} = \sum_n A_n^s f_n^{\pm}$ with s denoting the solution order and A_n^s its corresponding eigenvector components. Only the lowest state $s = 1$ is of interest here.

Before proceeding to numerical applications, it is worth to mention few aspects of the adopted approximation. As the angular momentum increases, the minima of the original $u_L(\phi)$ potential become sharper and move to higher values of

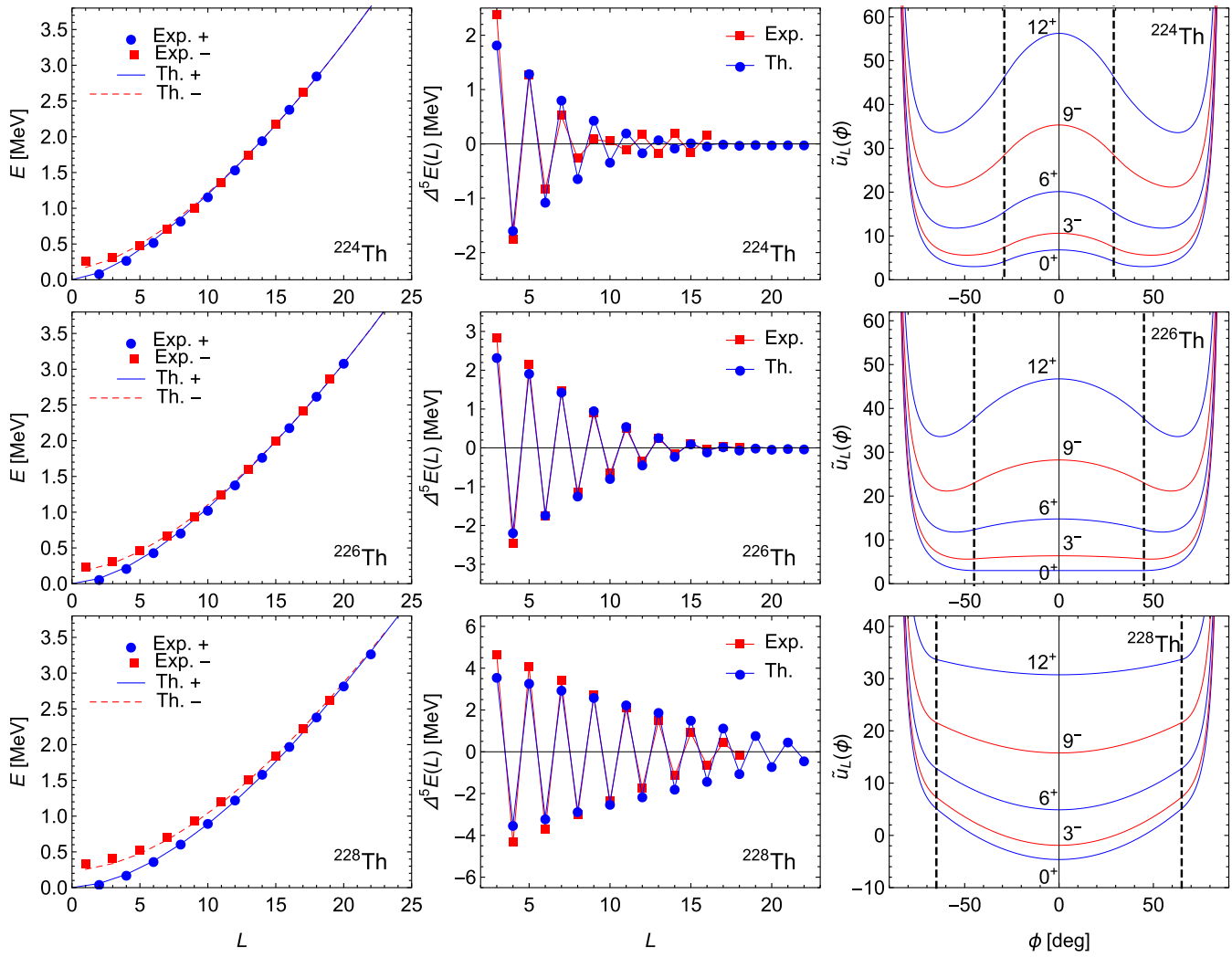

FIG. 4. Same as in Fig. 3, but for ^{224}Th [42], ^{226}Th [48], and ^{228}Th [46].

ϕ. For $L = 0$ the minimum position is at $\phi_0 = 45^\circ$ [23]. If we restrict ourselves to $|\phi_c| < 45^\circ$, the position and elevation of the potential minima from $u_L(\phi)$ are preserved in $\tilde{u}_L(\phi)$. Going further with $|\phi_c| > 45^\circ$ will result in negative values of a coming from the conditions (2.10), and the lowest L potentials $\tilde{u}_L(\phi)$ will then exhibit a single central minimum. This situation increases the energy splitting and is consistent with the octupole vibration mechanism. The critical angular momentum L_c, marking the transition from single to double well shape of the $\tilde{u}_L(\phi)$ potential, increases with $|\phi_c|$. At sufficiently high $|\phi_c|$ values, the $\tilde{u}_L(\phi)$ potential acquires a single well shape for the hole considered range of angular momentum as is depicted in Fig. 1. Note, however, that due to the matching point conditions, the single well becomes shallower with increasing angular momentum.

The numerical values of $W_L^{\pm}$ will acquire negative values for large $|\phi_c|$, as the potential deepens. In this case, w_0 will be used to counterbalance the overall centrifugal contribution in order to have a $\tilde{\beta}$ equation bounded below. Similarly, w_0 is also allowed to have negative values for tempering the increased rotational contribution due to the finite barrier.

C. The $\tilde{\beta}$ equation

If one considers a harmonic oscillator (HO) potential $u(\tilde{\beta}) = \tilde{\beta}^2$ in Eq. (2.6) for the $\tilde{\beta}$ shape variable, one can solve it analytically. Then the total energy is readily obtained as

$$E_{\rm Ln}^{\pm} = \frac{\hbar^2}{2B}\epsilon_{\rm Ln} = \frac{\hbar^2}{B}(2n + \nu_L^{\pm} + 1) \tag{2.14}$$

with the corresponding wave function

$$\psi_{\rm Ln}^{\pm}(\tilde{\beta}) = \sqrt{\frac{2n!}{\Gamma(n + \nu_L^{\pm} + 1)}}\tilde{\beta}^{\nu_L^{\pm}} L_n^{\nu_L^{\pm}}(\tilde{\beta}^2) e^{-\tilde{\beta}^2/2}, \tag{2.15}$$

where

$$\nu_L^{\pm} = \sqrt{W_L^{\pm} + w_0}, \tag{2.16}$$

and $n = 0, 1, 2, \ldots$ with $n = 0$ denoting the positive and negative parity ground state band. When $w_0 > 0$, the total potential $u(\tilde{\beta}, \phi) = \tilde{\beta}^2 + w_0/\tilde{\beta}^2$ obtained after the adopted approximation in the ϕ equation, acquires the form of the Davidson potential used for example in Refs. [19,22,25,26] for the

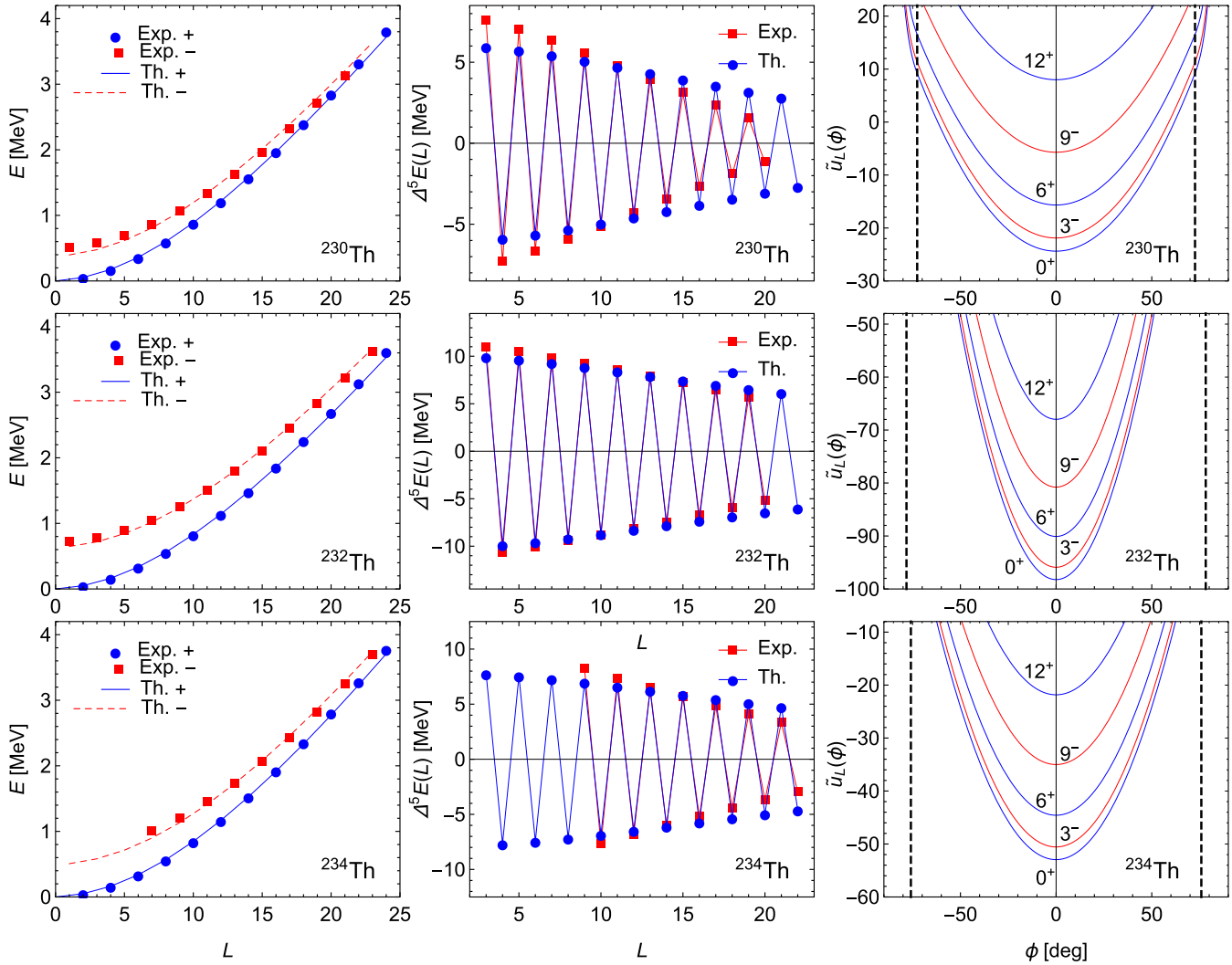

FIG. 5. Same as in Fig. 3, but for ^{230}Th [49], ^{232}Th [50], and ^{234}Th [52].

octupole collective excitations. Similarly, if one considers a hyperbolic potential $u(\tilde{\beta}) = -1/\tilde{\beta}$, the results for energy

$$E^{\pm}_{\rm Ln} = -\frac{\hbar^2(\eta^{\pm}_L)^2}{2B} = -\frac{\hbar^2}{8B}\frac{1}{\left(\nu^{\pm}_L + \frac{1}{2} + n\right)^2}, \tag{2.17}$$

and wave function

$$\psi^{\pm}_{\rm Ln}(\tilde{\beta}) = (2\eta^{\pm}_L)^{\nu^{\pm}_L+1}\sqrt{\frac{n!}{\Gamma(n+2\nu^{\pm}_L+1)(2n+2\nu^{\pm}_L+1)}} \times e^{-\eta^{\pm}_L\tilde{\beta}}\tilde{\beta}^{\nu^{\pm}_L}L_n^{2\nu^{\pm}_L}(2\eta^{\pm}_L\tilde{\beta}), \tag{2.18}$$

would be equivalent to those for a Kratzer potential $u(\tilde{\beta},\phi) = -1/\tilde{\beta} + w_0/\tilde{\beta}^2$ which is customarily employed in quadrupole collective models [27–30], but not yet considered for the octupole degrees of freedom. The notations are kept the same as in the HO case.

The set of parameter free solvable potentials is completed with the infinite square well potential (ISW):

$$u(\tilde{\beta}) = \begin{cases} 0, & \tilde{\beta} \leqslant 1 \\ \infty, & \tilde{\beta} > 1, \end{cases} \tag{2.19}$$

whose energy is well known

$$E^{\pm}_{\rm Ln} = \frac{\hbar^2}{2B}\left[x_{n\nu^{\pm}_L}\right]^2 \tag{2.20}$$

with $x_{n\nu^{\pm}_L}$ being the $(n+1)$th root of Bessel function $J_{\nu^{\pm}_L}(\beta)$ used to define the corresponding wave function

$$\psi^{\pm}_{\rm Ln}(\tilde{\beta}) = \sqrt{2}\frac{J_{\nu^{\pm}_L}\left(x_{n\nu^{\pm}_L}\tilde{\beta}\right)}{J_{\nu^{\pm}_L+1}\left(x_{n\nu^{\pm}_L}\right)}. \tag{2.21}$$

By adding the centrifugal term $w_0/\tilde{\beta}^2 > 0$, one can move the inner wall of the ISW. This effect is similar to the confined β-soft model for the quadrupole deformation [31,32]. As a consequence, the Bessel function's order $\nu^{\pm}_L$ defined by Eq. (2.16) is increased due to the additional contribution of

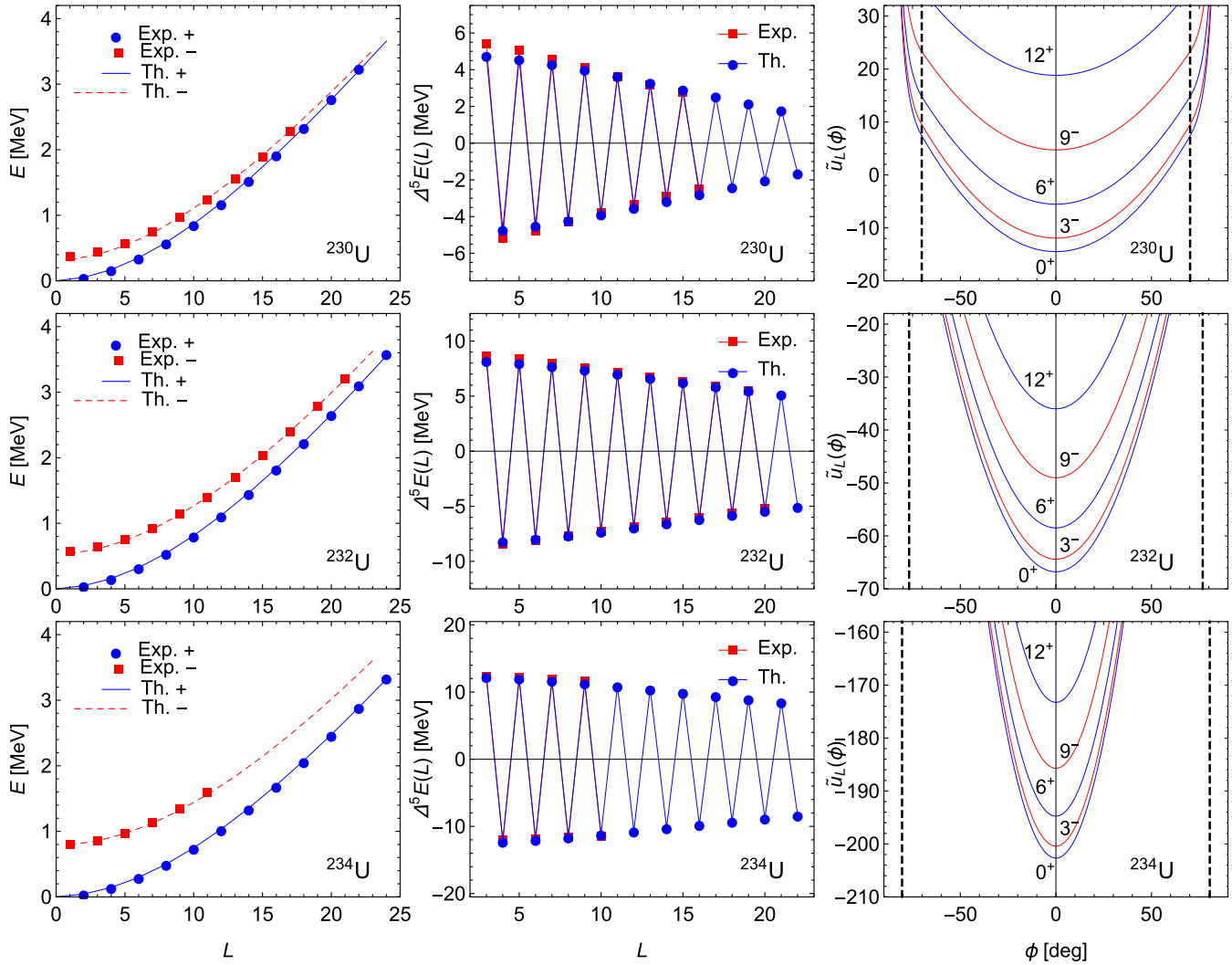

FIG. 6. Same as in Fig. 3, but for ^{230}U [49], ^{232}U [53], and ^{234}U [52].

ω_0. As in the cases of HO and hyperbolic potentials, the ω_0 parameter generalizes the total centrifugal contribution.

It is worth to mention that all considered potentials are scaled. More precisely, the string constant of the HO, the strength of the hyperbolic potential as well as the position of the infinite wall in ISW are set to unity, because their values just add a factor to the total energy assumed included in the mass B, and are not relevant for the normalized wave functions. Nevertheless, one must be aware that the scaling is different for each potential when these are compared to each other.

D. Electromagnetic transitions

The relevant electric transition probabilities can be written in the following form [22,23,25]:

$$B(E\lambda; Lnp \rightarrow L'n'p') = t_\lambda \left(C^{L\lambda L'}_{000}\right)^2 \left(\tilde{B}^\lambda_{Lnp;L'n'p'} I^\lambda_{Lp;L'p'}\right)^2, \quad \lambda = 1, 2, 3, \tag{2.22}$$

where t_λ are constants gathering the corresponding physical units and various normalization constants. In the above expression, C is the Clebsch-Gordan coefficient, $\tilde{B}$ is the integral over the $\tilde{\beta}$ variable,

$$\tilde{B}^1_{Lnp;L'n'p'} = \int \tilde{\beta}^3 \psi^p_{\mathrm{Ln}}(\tilde{\beta}) \psi^{p'}_{L'n'}(\tilde{\beta}) d\tilde{\beta}, \tag{2.23}$$

$$\tilde{B}^{2,3}_{Lnp;L'n'p'} = \int \tilde{\beta}^2 \psi^p_{\mathrm{Ln}}(\tilde{\beta}) \psi^{p'}_{L'n'}(\tilde{\beta}) d\tilde{\beta}, \tag{2.24}$$

while I is the integral over the angular variable ϕ:

$$I^1_{Lp;L'p'} = \int \sin 2\phi \chi^p_L(\phi) \chi^{p'}_{L'}(\phi) d\phi, \tag{2.25}$$

$$I^2_{Lp;L'p'} = \int \cos\phi \chi^p_L(\phi) \chi^{p'}_{L'}(\phi) d\phi, \tag{2.26}$$

$$I^3_{Lp;L'p'} = \int \sin\phi \chi^p_L(\phi) \chi^{p'}_{L'}(\phi) d\phi. \tag{2.27}$$

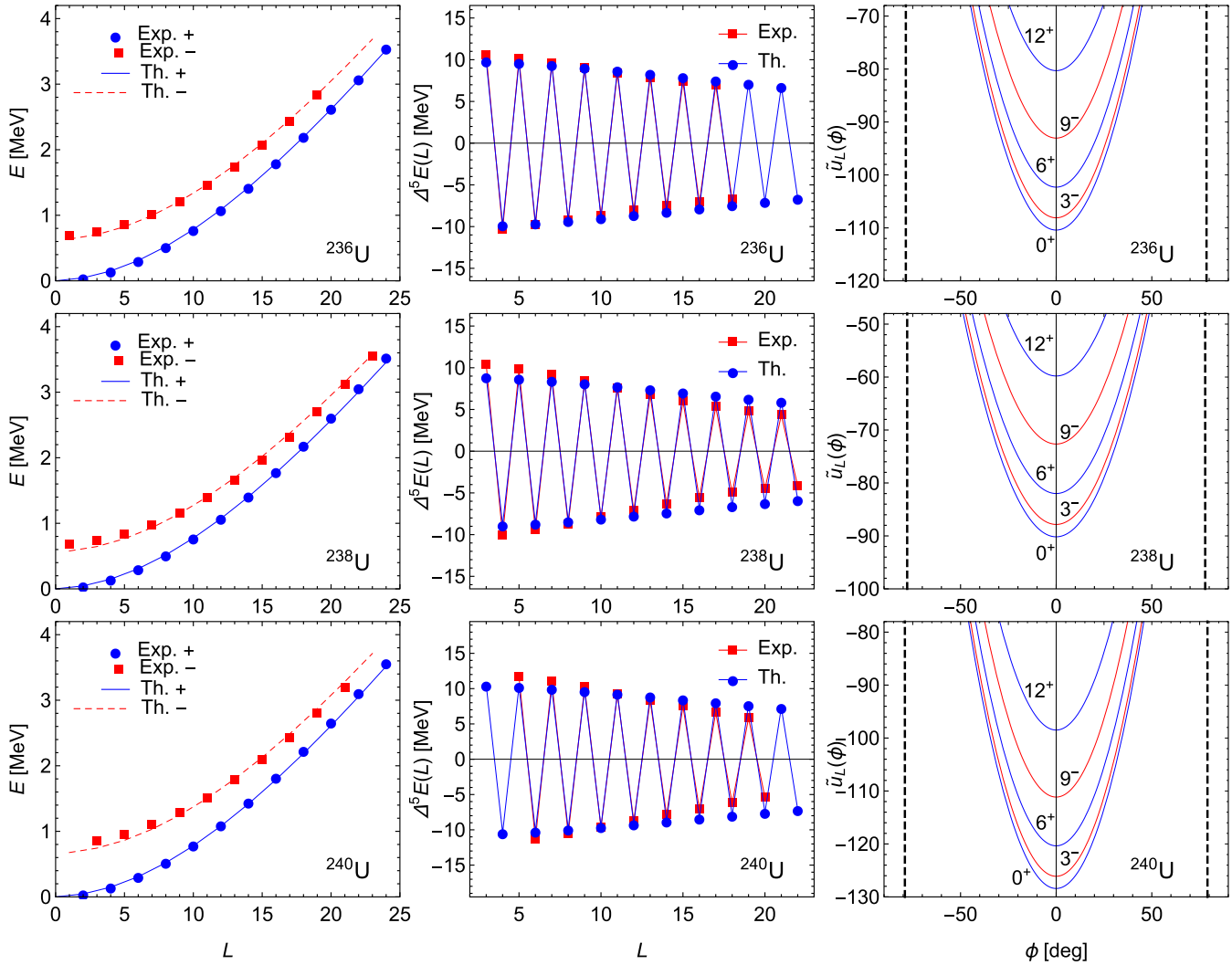

FIG. 7. Same as in Fig. 3, but for ^{236}U [54], ^{238}U [55], and ^{240}U [56].

III. NUMERICAL APPLICATION

The experimental realization of the proposed model is sought among Ra isotopes and light actinide nuclei, which exhibit the most extensive alternate parity bands and are well known examples of octupole deformation. The focus of the study is the yrast positive and negative parity states. Therefore, we fitted the corresponding experimental data only for these states from Ra, Th, U, and Pu isotopes, by minimizing the quantity

$$\sigma = \sqrt{\frac{1}{N}\sum_{\text{states}}^{N}\left(\frac{E_{\text{exp}}(L^{\pm})}{E_{\text{exp}}(2^{+})} - \frac{E^{\pm}_{L0} - E^{+}_{00}}{E^{+}_{20} - E^{+}_{00}}\right)^{2}}. \tag{3.1}$$

The fits on energy ratios have the advantage of eliminating the scale dependence on the mass B, leaving only two relevant parameters, $|\phi_c|$ and w_0. Although some nuclei have experimental data up to very high spin states, the fits and the associated analysis are limited to $L \leqslant 24$ states. The separation constant $W^{\pm}_L$ needed for the determination of the theoretical energies is obtained by diagonalizing Eq. (2.7) with the potential (2.11) in a basis of 100 $f^{\pm}_n(\phi)$ states which assures a comfortable convergence of the eigenvalues for all considered angular momentum values. The diagonalization procedure is applied for a grid of $|\phi_c|$ values of one degree increment in the interval $[2^{\circ}, 85^{\circ}]$. A fine tuning is performed for fits with $|\phi_c| > 70^{\circ}$. The same set of experimental data is fitted separately with total energy determined from HO, hyperbolic, and ISW $\tilde{\beta}$ potentials. It is found that the HO potential performs much better than the hyperbolic potential for the considered nuclei with the comparable performance only for the ^{240}U nucleus. We will further omit the results of the hyperbolic potential. However, one expects that it would fare better in the other regions of the nuclide chart with possible octupole deformation. For few lighter nuclei, the ISW model is the most suitable choice.

Excepting the lighter $A < 224$ isotopes of Ra and Th, the model fits are excellent for all experimentally available extended alternate parity bands in the investigated isotopic chains. This can be seen from the σ values reported in Table I for the best suited $\tilde{\beta}$ potential and the comparison between experimental and theoretical energy spectra

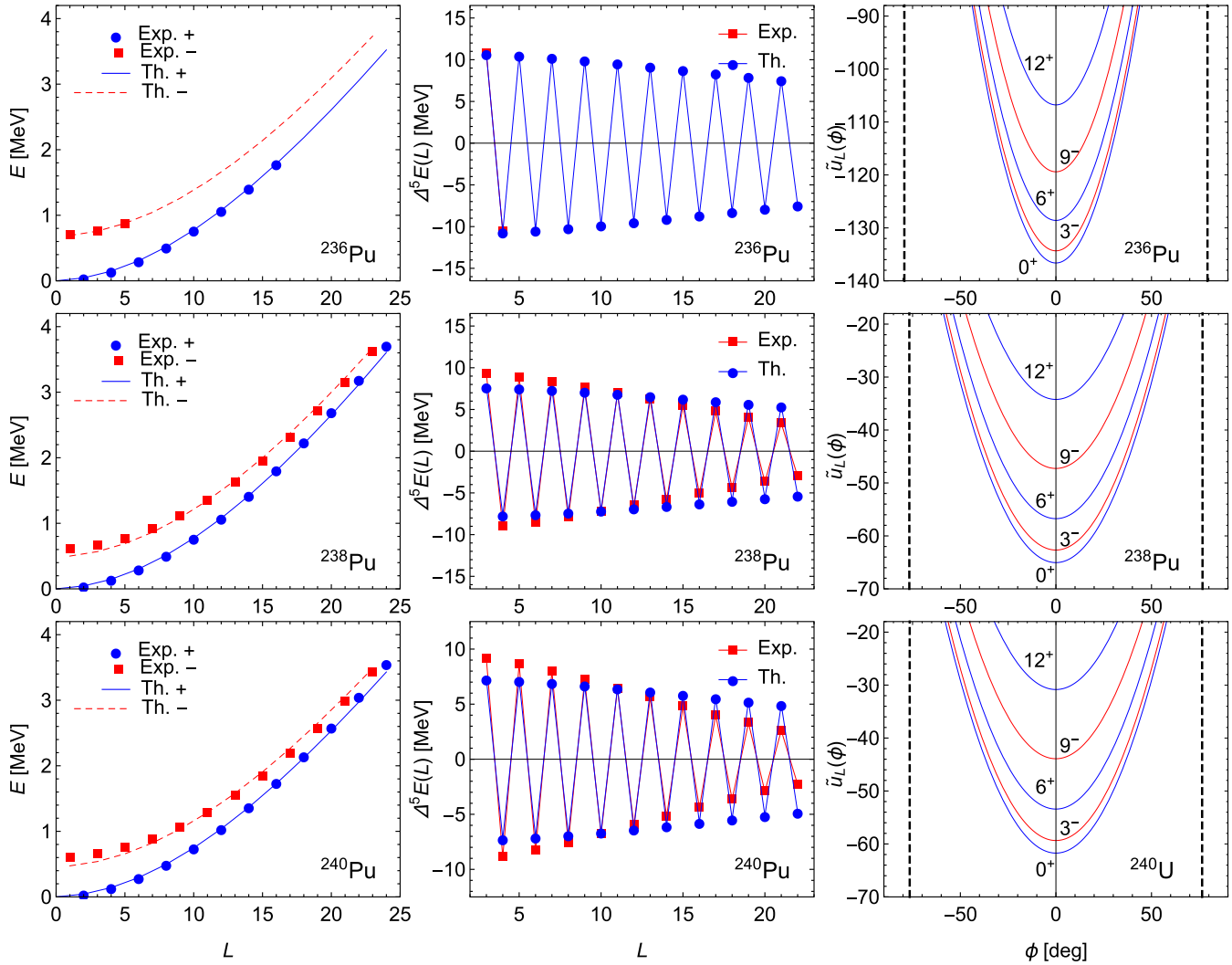

FIG. 8. Same as in Fig. 3, but for ^{236}Pu [54], ^{238}Pu [55], and ^{240}Pu [57].

visualized in Figs. 3–8. The agreement with absolute energy levels can be easily ascertained by factorizing σ with the excitation energy of the experimental 2^+ state also listed in Table I. The ^{234}Th and ^{240}U nuclei lack experimental data for the negative parity band head state. As the theoretical results in general underestimate the experimental data in the low spin region of the negative parity band, the predicted elevation of 1^- state at 507.5 keV for ^{234}Th and 676.9 keV for ^{240}U can be considered as reference lower limits for future measurements.

The energy splitting between alternate parity bands produces the so-called odd-even or $\Delta L = 1$ staggering. A suitable measure of this effect is the fifth order finite difference of $E(L)$ [33,34]:

$$\Delta^5 E(L) = 6\Delta E(L) - 4\Delta E(L-1) - 4\Delta E(L+1) + \Delta E(L+2) + \Delta E(L-2), \quad (3.2)$$

where $\Delta E(L) = E(L) - E(L-1)$ and E denotes experimental or theoretical energies. The extreme sensibility of this quantity is often used to study the fine structure of the octupole bands. For example, the different inertia of the positive and negative parity bands were shown to produce the unusual beat patterns in the $\Delta L = 1$ staggering [33–35]. As can be seen from Figs. 3 and 4, such an effect is most obvious in ^{224}Ra, ^{226}Ra, and ^{224}Th nuclei. To reproduce this behavior, a more consistent treatment of the quadrupole-octupole rotation is necessary [35–37]. Nevertheless, the present simple model reproduces very well the angular momentum where energy splitting disappears for these three nuclei, and the general staggering behavior for the other nuclei with a strong octupole vibration nature (see Figs. 5–8).

The proposed model can be in principle used to describe excited alternate parity bands. Considering $n = 1$ for the $\tilde{\beta}$ vibration quanta, we made in Table II some predictions for the band heads of $K = 0$ excited alternate parity bands. The considered nuclei are known as good rotors, therefore vibrational excited states are expected at very high energy. Apart from the lightest Ra and Th isotopes, where the theory conforms well with the yrare experimental 0^+ and 1^- states, the theory predicts very high band heads, especially for the negative

TABLE II. Theoretical excited band head states 0^+ and 1^- are compared with possible experimental realizations in the considered nuclei.

Nucleus	$E_{th}(0_2^+)$ [keV]	$E_{\exp}(0_{i>1}^+)$ [keV]	$E_{th}(1_2^-)$ [keV]	$E_{\exp}(1_{i>1}^-, K=0)$ [keV]
^{224}Ra [42]	802.6	916.4	1067.3	1053.0
^{226}Ra [48]	755.6	824.6	1099.9	1077.2
^{228}Ra [46]	1047.6	721.2	1405.2	
		1042.0		
^{224}Th	803.6		1105.5	
^{226}Th [48]	969.7	805.2	1274.3	
^{228}Th [46]	892.2	831.8	1307.0	
^{230}Th [49]	1215.6	634.9	1612.9	
^{232}Th [51]	1222.2	730.4	1869.4	1303.3
		1078.5		1489.0
^{234}Th [52]	1346.6	810.0	1854.2	
		1470.0		
^{230}U	1208.0		1530.3	
^{232}U [50]	1294.0	691.4	1830.5	
		927.3		
		1277.2		
^{234}U [52]	1278.5	809.9	2070.5	1237.3
		1044.5		1809.7
				1969.9
^{236}U [54]	1383.2	919.1	2020.5	2086.5
^{238}U [55]	1326.2	927.2	1904.5	1996.7
		997.2		
^{240}U	1396.6		2073.5	
^{236}Pu	1425.9		2117.1	
^{238}Pu [55]	1549.4	962.8	2049.3	1447.2
		1134.0		1621.3
		1228.7		1636.4
		1426.6		
^{240}Pu [57]	1407.9	860.7	1881.5	1607.7
		1089.5		1775.3
		1525.9		1917.8

parity in strongly vibrational nuclei. Nevertheless, Table II shows some possible experimental realizations of these states in higher order 0^+ and 1^- measured energy levels.

The two parameters of the model have clear physical attributes: $|\phi_c|$ mediates between stable octupole deformation and octupole vibration modes, while w_0 is a measure of the overall rotational behavior. The Ra and Th nuclei with $A = 224, 226$, and 228, have visibly lower values for both parameters than the rest of the considered nuclei. As can be seen in Figs. 3 and 4, the lower and moderate values of $|\phi_c|$ are reflected in a double well shape of their corresponding $\tilde{u}_L(\phi)$ potential, sustained in the whole range of the considered angular momentum states ($A = 224$) or attained at higher spins ($A = 226, 228$). The double well shape of the $\tilde{u}_L(\phi)$ potential is associated with a stable admixture of octupole and quadrupole deformation, while a single well $\tilde{u}_L(\phi)$ potential obtained for the rest of the considered nuclei is associated with the octupole vibration which commences through the central value $\phi = 0$ where octupole deformation vanishes. An interesting situation arises for ^{226}Th, where the ground state $\tilde{u}_L(\phi)$ potential is completely flat.

The deduced values of the both parameters listed in Table I have a regular evolution with nucleon numbers. For example, Ra and Th nuclei with $A = 224, 226$, and 228 exhibit the same increasing behavior for both $|\phi_c|$ and w_0. As a matter of fact, these particular Ra and Th isotopes were proposed as critical points for shape and dynamical phase transitions [9,10,20–23,25,38]. It is not surprising then that ISW potential usually employed in critical phenomena is better suited for ^{224,226}Ra and ^{224,226,228}Th. These nuclei are indeed special also from the angular variable's point of view. The relatively small $|\phi_c|$ value of $A = 226$ isotopes allows a sufficient amount of tunneling to raise the negative parity states with $L \leqslant 3$ above the separation barrier. One can say that in these nuclei takes place a transition from a delocalized to a stable quadrupole-octupole deformation. While the ^{226,228}Ra and ^{226,228}Th nuclei contain the dynamical (spin-dependent) transition from a single to a double well potential associated to the change from an octupole vibration mode to an increasingly stabilized octupole deformation. This transition commences through different quantum phases: starting with single well vibration, then a double well vibration with energy above the separation barrier which changes to a tunneling vibration and finally ending in a stable quadrupole-octupole phase where the two $\pm\phi$ configurations no longer interact. A similar picture is present for example in the chiral bands of triaxial nuclei, where the dynamical transition changes the chiral vibration into static chirality of the particle-rotor configuration [39,40]. Considering the changes in the equilibrium shape, it can be said that $A = 226, 228$ Ra and Th nuclei are perfect examples of the Poincaré shape transition [41]. The model also suggests a transition from a $\tilde{\beta}$ potential with a softer inner wall (ISW) to one with a softer outer wall (HO) between ^{226}Ra and ^{228}Ra, as well as between ^{228}Th and ^{230}Th. The heavier Th nuclei continue the increasing trend of both parameters up to a maximum at neutron number $N = 142$, which is mirrored by the parameters obtained for U and Pu isotopes.

It is well known that the transition probabilities are more sensible to structural changes. The calculated values of the intraband $E2$ transition probabilities listed in Tables III and IV, strengthen the observations regarding the different nature of the $A = 224, 226, 228$ Ra and Th isotopes. Both theoretical and experimental transition rates are normalized such that to exclude the scale dependence on t_2. This is achieved by presenting the data in terms of ratios $B(E2, L^p \to L^p - 2)/B(E2, 2^+ \to 0^+)$. A similar presentation is used also for $E1$ and $E3$ data, by considering ratios of transition rates with the same multipolarity. While for the octupole vibrational nuclei $A > 228$ is predicted a monotonously increasing trend for the $B(E2, L^p \to L^p - 2)$ confirmed by the available experimental data, the lightest Ra and Th nuclei have a rather different evolution with spin of this quantity. Indeed, the calculated transitions for $A = 224$ and 226 isotopes show a moderate increase for few angular momentum states and then they start to decrease towards a saturation value at high spins, which is lower for the critical $A = 226$ nuclei. The evolution with spin of the $E2$ rates for the $A = 228$ isotopes is apparently similar

TABLE III. Theoretical and experimentally available $E2$ transition probabilities in units of $B(E2; 2^+ \rightarrow 0^+)$ for ^{224,226,228}Ra [42,43,45,47] and $^{224-234}$Th [46,50] nuclei.

	^{224}Ra		^{226}Ra		^{228}Ra		^{224}Th		^{226}Th		^{228}Th		^{230}Th		^{232}Th		^{234}Th	
$L_i^p \rightarrow L_f^p$	Th.	Exp.	Th.	Exp.	Th.	Exp	Th.	Exp.	Th.	Exp.	Th.	Exp	Th.	Exp.	Th.	Exp.	Th.	Exp.
$4^+ \rightarrow 2^+$	1.46	1.41(8)	1.49	1.49^{+7}_{-4}	1.47	1.47(16)	1.48		1.45		1.47	1.45(7)	1.45		1.45	1.44(15)	1.45	
$6^+ \rightarrow 4^+$	1.59	1.59(14)	1.72	1.76^{+4}_{-5}	1.70	1.77(20)	1.64		1.61		1.69		1.65		1.64	1.65(14)	1.63	
$8^+ \rightarrow 6^+$	1.57	1.72(51)	1.84	1.69^{+4}_{-6}	1.89	1.80(20)	1.63		1.63		1.85		1.79		1.78	1.74(12)	1.76	
$10^+ \rightarrow 8^+$	1.47		1.86	1.63^{+13}_{-6}	2.08	2.36^{+27}_{-25}	1.53		1.54		1.96		1.93		1.91	1.83(15)	1.87	
$12^+ \rightarrow 10^+$	1.35		1.77	3.17^{+15}_{-26}	2.26	1.77^{+27}_{-17}	1.42		1.36		2.04		2.06		2.05	1.87(18)	1.99	
$14^+ \rightarrow 12^+$	1.24		1.57	1.81^{+26}_{-11}	2.45		1.31		1.18		2.07		2.20		2.19	1.97(19)	2.11	
$16^+ \rightarrow 14^+$	1.16		1.35	2.00^{+100}_{-29}	2.64		1.23		1.05		2.04		2.35		2.33	1.97(23)	2.24	
$18^+ \rightarrow 16^+$	1.09		1.17	0.83^{+24}_{-17}	2.80		1.16		0.95		1.94		2.50		2.49	2.27(38)	2.37	
$20^+ \rightarrow 18^+$	1.03		1.03		2.93		1.09		0.88		1.74		2.65		2.64	1.82(32)	2.50	
$22^+ \rightarrow 20^+$	0.98		0.94		2.98		1.04		0.82		1.49		2.79		2.81	2.12(57)	2.64	
$24^+ \rightarrow 22^+$	0.93		0.87		2.92		0.98		0.78		1.24		2.93		2.98	1.21(36)	2.78	
$3^- \rightarrow 1^-$	1.01	0.95(10)	0.98	1.87^{+6}_{-12}	1.08		1.04		0.94		1.01		1.11		1.28		1.18	
$5^- \rightarrow 3^-$	1.21	1.94(62)	1.18	1.49^{+4}_{-7}	1.30		1.26		1.11		1.21		1.33		1.54		1.41	
$7^- \rightarrow 5^-$	1.29		1.27	1.08^{+2}_{-4}	1.44		1.35		1.18		1.32		1.46		1.68		1.54	
$9^- \rightarrow 7^-$	1.31		1.31	1.53^{+2}_{-9}	1.56		1.38		1.19		1.38		1.56		1.79		1.64	
$11^- \rightarrow 9^-$	1.29		1.31	1.95^{+18}_{-38}	1.68		1.36		1.16		1.42		1.65		1.90		1.73	
$13^- \rightarrow 11^-$	1.24		1.27	3.63^{+84}_{-49}	1.78		1.31		1.11		1.43		1.75		2.01		1.82	
$15^- \rightarrow 13^-$	1.18		1.20	2.97^{+212}_{-119}	1.88		1.25		1.04		1.41		1.84		2.13		1.91	
$17^- \rightarrow 15^-$	1.12		1.12		1.95		1.18		0.97		1.36		1.93		2.25		2.01	
$19^- \rightarrow 17^-$	1.06		1.04		2.01		1.12		0.90		1.30		2.01		2.38		2.11	
$21^- \rightarrow 19^-$	1.00		0.96		2.03		1.06		0.85		1.21		2.09		2.51		2.21	
$23^- \rightarrow 21^-$	0.95		0.89		2.02		1.01		0.80		1.11		2.15		2.64		2.31	

TABLE IV. Same as in Table III, but for $^{230-240}$U [54,55] and ^{236,238,240}Pu nuclei.

	^{230}U		^{232}U		^{234}U		^{236}U		^{238}U		^{240}U		^{236}Pu		^{238}Pu		^{240}Pu	
$L_i^p \rightarrow L_f^p$	Th.	Exp.	Th.	Exp.	Th.	Exp	Th.	Exp.	Th.	Exp.	Th.	Exp	Th.	Exp.	Th.	Exp.	Th.	Exp.
$4^+ \rightarrow 2^+$	1.45		1.45		1.45		1.44	1.43(11)	1.44		1.44		1.44		1.44		1.44	
$6^+ \rightarrow 4^+$	1.64		1.63		1.62		1.62	1.54(11)	1.62		1.62		1.62		1.61		1.61	
$8^+ \rightarrow 6^+$	1.78		1.76		1.75		1.74	1.56(17)	1.75	1.46(21)	1.74		1.73		1.72		1.73	
$10^+ \rightarrow 8^+$	1.90		1.88		1.86		1.85	1.44(17)	1.85	1.71(21)	1.84		1.84		1.81		1.82	
$12^+ \rightarrow 10^+$	2.03		1.99		1.97		1.95	1.64(29)	1.96	1.78(18)	1.94		1.93		1.89		1.91	
$14^+ \rightarrow 12^+$	2.15		2.12		2.08		2.05	1.80(21)	2.07	1.75(14)	2.05		2.03		1.98		2.01	
$16^+ \rightarrow 14^+$	2.27		2.24		2.20		2.16	1.52(17)	2.19	1.74(8)	2.16		2.14		2.07		2.11	
$18^+ \rightarrow 16^+$	2.39		2.37		2.33		2.28	1.96(21)	2.31	1.71(11)	2.27		2.25		2.16		2.21	
$20^+ \rightarrow 18^+$	2.49		2.51		2.46		2.40	2.04(33)	2.43	1.64(14)	2.39		2.36		2.26		2.31	
$22^+ \rightarrow 20^+$	2.57		2.65		2.59		2.53	2.08(49)	2.56	1.74(27)	2.51		2.48		2.36		2.42	
$24^+ \rightarrow 22^+$	2.60		2.80		2.73		2.66	2.68(53)	2.69	1.89(30)	2.64		2.61		2.46		2.53	
$3^- \rightarrow 1^-$	1.05		1.21		1.33		1.25		1.23		1.26		1.26		1.17		1.17	
$5^- \rightarrow 3^-$	1.25		1.45		1.59		1.49		1.47		1.50		1.50		1.39		1.39	
$7^- \rightarrow 5^-$	1.37		1.57		1.73		1.62		1.60		1.63		1.63		1.50		1.51	
$9^- \rightarrow 7^-$	1.45		1.68		1.83		1.71		1.69		1.73		1.73		1.58		1.59	
$11^- \rightarrow 9^-$	1.53		1.77		1.93		1.80		1.78		1.82		1.81		1.65		1.67	
$13^- \rightarrow 11^-$	1.60		1.87		2.02		1.89		1.87		1.91		1.90		1.72		1.74	
$15^- \rightarrow 13^-$	1.66		1.96		2.12		1.98		1.96		1.99		1.98		1.79		1.82	
$17^- \rightarrow 15^-$	1.72		2.07		2.23		2.07		2.06		2.09		2.07		1.86		1.90	
$19^- \rightarrow 17^-$	1.76		2.17		2.33		2.17		2.16		2.18		2.17		1.94		1.97	
$21^- \rightarrow 19^-$	1.78		2.28		2.45		2.27		2.26		2.28		2.27		2.01		2.06	
$23^- \rightarrow 21^-$	1.78		2.39		2.56		2.37		2.37		2.39		2.37		2.09		2.14	

TABLE V. Theoretical and experimentally available $E1$ transition probabilities in 10^{-5} W.u. for ^{224}Ra [43], ^{226}Ra [45], ^{228}Ra [47], ^{232}Th [58], and ^{240}Pu [57]. The underlined experimental value is used for fixing the t_1 factor from Eq.(2.22) by equating it with the corresponding theoretical estimation.

	^{224}Ra		^{226}Ra		^{228}Ra		^{232}Th		^{240}Pu	
$L_i^p \to L_f^p$	Th.	Exp.	Th.	Exp.	Th.	Exp.	Th.	Exp.	Th.	Exp.
$1^- \to 0^+$	2.7	<5	35	<u>35</u>(13)	27	$\underline{27}^{+52}_{-20}$	8.7		2.2	
$1^- \to 2^+$	5.9	<13	75	64(19)	56	13^{+23}_{-9}	17.7		4.5	
$3^- \to 2^+$	3.9	$\underline{3.9}^{+17}_{-14}$	49	22(5)	36	48^{+54}_{-33}	11.5		2.9	
$3^- \to 4^+$	6.1		73	19(3)	52	39^{+43}_{-19}	15.8		3.9	
$5^- \to 4^+$	5.0	4^{+3}_{-2}	59	33(5)	42	66^{+73}_{-49}	12.7		3.2	>2.4
$5^- \to 6^+$	7.1		82		55		16.0	4.3(10)	3.9	><u>3.9</u>
$7^- \to 6^+$	6.3	<30	72	69(9)	49	19^{+43}_{-15}	13.9		3.4	
$7^- \to 8^+$	8.4		96	123(94)	63		16.9	10.7(20)	4.0	
$9^- \to 8^+$	7.7		86	127(21)	58	90^{+27}_{-6}	15.3		3.6	
$9^- \to 10^+$	9.6		114	160(59)	73		18.3	<u>18.3</u>(27)	4.2	
$11^- \to 10^+$	8.9		104	198(48)	69		17.0		3.9	
$11^- \to 12^+$	10.4		136	223(102)	86		20.0	18(5)	4.5	
$13^- \to 12^+$	9.7		126	615(156)	83		19.0		4.2	
$13^- \to 14^+$	10.8		158	654^{+302}_{-101}	103		22.2		4.8	
$15^- \to 14^+$	10.2		147	408^{+104}_{-208}	100		21.3		4.6	

to that of the heavier nuclei. One can observe however that it starts to decrease at very high spins, where these nuclei start to acquire a more stable octupole deformation. The available experimental data for these lighter nuclei confirm mainly the increasing part of the theoretical evolution with spin. With the exception of ^{226}Ra nucleus, where the experimental data shows a maximum in the vicinity of the predicted maximal transition rate, the decreasing region of interest in other nuclei is not explored or has data with large uncertainties.

The trends in $E1$ transition rates are more erratic to be systematically compared. Therefore, we used the available experimental information on these transitions to rather check the model's performance. From Table V, one can see that the general increase with spin is reproduced by the theory with few occasional data matches with extrapolated theoretical values. An important characteristic of the theoretical $E1$ rates is the fact that $B(E1; L^- \to (L+1)^+)/(E1; L^- \to (L-1)^+) > 1$ is preserved for all spins. This rule is satisfied also within experimental data complemented by experimentally available ratios shown in Table VI with few exceptions in low spin transitions of ^{226,228}Ra nuclei which due to large uncertainties can very well confirm the rule.

In what concerns $E3$ transition probabilities, the experimental data are scarce. There are however few nuclei with sufficient data to be compared with model predictions. Thus, for ^{224}Ra nucleus the measured $B(E3; 1^- \to 2^+)/B(E3; 3^- \to 0^+) = 5(1)$ and $B(E3; 5^- \to 2^+)/B(E3; 3^- \to 0^+) = 1.45(42)$ ratios [43] are consistent with the theoretical values 3.21 and, respectively, 1.68. Also, combining the results of Refs. [54,59] for ^{236}U, one finds that the deduced experimental ratio $B(E3; 0^+ \to 3^-)/B(E3; 1^- \to 4^+) = 2.58(51)$ is comparable with the theoretical value 1.71.

IV. CONCLUSIONS

A model based on the quadrupole-octupole axially symmetric version of the general Bohr Hamiltonian is constructed by means of a consistent treatment of the interaction between configurations with opposite octupole deformation. The interaction is modeled by a finite barrier in the angular variable mediating the relative contribution between quadrupole and octupole deformations, whose spin dependence is naturally given by the inner geometry of the shape parametrization.

TABLE VI. Theoretical and experimentally available ratios $B(E1; L^- \to (L+1)^+)/(E1; L^- \to (L-1)^+)$ for ^{226}Th [20], ^{230}Th [58], ^{236}U [54], ^{238}U [55].

	^{226}Th		^{230}Th		^{236}U		^{238}U	
L^-	Th.	Exp.	Th.	Exp.	Th.	Exp.	Th.	Exp.
1^-	2.11	1.85(17)	2.03	2.28(12)	2.02	2.15(33)	2.02	1.57(79)
3^-	1.49	1.01(26)	1.38	1.97(9)	1.36		1.37	
5^-	1.40		1.27	2.21(11)	1.24		1.24	
7^-	1.37		1.22	2.41(13)	1.19		1.20	

The resulted model has only two adjustable parameters up to a scale. Numerical applications on extended alternate parity bands in Ra, Th, U, and Pu nuclei demonstrate the model's ability to describe in a unified manner the evolution of the octupole deformation from a vibrational type to a stable one, within an isotopic chain, as well as a function of spin within the rotational bands of certain nuclei. As a result, we identified the Ra and Th nuclei with $A = 224, 226, 228$, as belonging to the critical region of the shape phase transition between stable and dynamic octupole deformation. The extension of the critical region over few nuclei is due to its spin dependence. More precisely, $A = 224$ nuclei have an incipient stable octupole deformation in their ground state with small mixing between positive and negative octupole deformation configurations, which rapidly vanishes into a well stabilized octupole deformation at high spins. The next $A = 226$ nuclei exhibit a clear transition at moderate spins from a highly anharmonic octupole vibration towards a static octupole deformation. This dynamical transition is moved at higher spins in the $A = 228$ nuclei, such that their ground and low spin states correspond to well behaved octupole vibration. It is worth mentioning that the model performs well also in U and Pu nuclei with a strong octupole vibration character.

The model predicts some specific trends in the electromagnetic properties of the suggested transitional nuclei, which must be confirmed by experimental measurements. The reliability of the predictions is supported by the reproduction of the available data on experimental $E1$, $E2$, and $E3$ transition probabilities. The successful reproduction of the spectral observables in such a various set of nuclei is used to extend the model calculations to excited alternate parity bands, for which one provided possible experimental counterparts.

ACKNOWLEDGMENTS

This work was supported by a grant of the Ministry of Research, Innovation and Digitalization, CNCS - UEFISCDI, Project No. PN-III-P1-1.1-TE-2021-0109, within PNCDI III.

[1] A. Bohr and B. R. Mottelson, *Nuclear Structure*, Vol. 2 (Benjamin, Reading, MA, 1975).
[2] L. M. Robledo and G. F. Bertsch, Phys. Rev. C **84**, 054302 (2011).
[3] P. A. Butler, J. Phys. G: Nucl. Part. Phys. **43**, 073002 (2016).
[4] Y. Cao, S. E. Agbemava, A. V. Afanasjev, W. Nazarewicz, and E. Olsen, Phys. Rev. C **102**, 024311 (2020).
[5] S. Frauendorf, Rev. Mod. Phys. **73**, 463 (2001).
[6] P. A. Butler *et al.*, Nat. Commun. **10**, 2473 (2019).
[7] S. Rohozinski, Rep. Prog. Phys. **51**, 541 (1988).
[8] P. A. Butler and W. Nazarewicz, Rev. Mod. Phys. **68**, 349 (1996).
[9] K. Nomura, D. Vretenar, T. Nikšić, and B.-N. Lu, Phys. Rev. C **89**, 024312 (2014).
[10] S. E. Agbemava, A. V. Afanasjev, and P. Ring, Phys. Rev. C **93**, 044304 (2016).
[11] P. Möller, R. Bengtsson, B. G. Carlsson, P. Olivius, T. Ichikawa, H. Sagawa, and A. Iwamoto, At. Data Nucl. Data Tables **94**, 758 (2008).
[12] H. J. Daley and F. Iachello, Ann. Phys. (NY) **167**, 73 (1986).
[13] J. Engel and F. Iachello, Nucl. Phys. A **472**, 61 (1987).
[14] B. Buck, A. C. Merchant, and S. M. Perez, Phys. Rev. C **57**, R2095 (1998).
[15] T. M. Shneidman, G. G. Adamian, N. V. Antonenko, R. V. Jolos, and W. Scheid, Phys. Rev. C **67**, 014313 (2003).
[16] W. Donner and W. Greiner, Z. Phys. **197**, 440 (1966).
[17] P. O. Lipas and J. P. Davidson, Nucl. Phys. **26**, 80 (1961).
[18] A. Ya. Dzyublik and V. Yu. Denisov, Yad. Fiz. **56**, 30 (1993).
[19] V. Yu. Denisov and A. Ya. Dzyublik, Nucl. Phys. A **589**, 17 (1995).
[20] P. G. Bizzeti and A. M. Bizzeti-Sona, Phys. Rev. C **70**, 064319 (2004).
[21] P. G. Bizzeti and A. M. Bizzeti-Sona, Eur. Phys. J. A **20**, 179 (2003).
[22] D. Bonatsos, D. Lenis, N. Minkov, D. Petrellis, and P. Yotov, Phys. Rev. C **71**, 064309 (2005).
[23] D. Lenis and D. Bonatsos, Phys. Lett. B **633**, 474 (2006).
[24] M. S. Nadirbekov, G. A. Yuldasheva, and V. Yu. Denisov, Phys. At. Nucl. **78**, 215 (2015).
[25] D. Bonatsos, A. Martinou, N. Minkov, S. Karampagia, and D. Petrellis, Phys. Rev. C **91**, 054315 (2015).
[26] N. Minkov, P. Yotov, S. Drenska, W. Scheid, D. Bonatsos, D. Lenis, and D. Petrellis, Phys. Rev. C **73**, 044315 (2006).
[27] L. Fortunato and A. Vitturi, J. Phys. G: Nucl. Part. Phys. **29**, 1341 (2003).
[28] D. Bonatsos, P. E. Georgoudis, N. Minkov, D. Petrellis, and C. Quesne, Phys. Rev. C **88**, 034316 (2013).
[29] A. I. Budaca and R. Budaca, Phys. Rev. C **101**, 064318 (2020).
[30] M. Chabab, I. El-ilali, A. Lahbas, and M. Oulne, Int. J. Mod. Phys. E **30**, 2150095 (2021).
[31] N. Pietralla and O. M. Gorbachenko, Phys. Rev. C **70**, 011304(R) (2004).
[32] D. Bonatsos, D. Lenis, N. Pietralla, and P. A. Terziev, Phys. Rev. C **74**, 044306 (2006).
[33] D. Bonatsos, C. Daskaloyannis, S. B. Drenska, N. Karoussos, N. Minkov, P. P. Raychev, and R. P. Roussev, Phys. Rev. C **62**, 024301 (2000).
[34] H. Ganev, V. P. Garistov, and A. I. Georgieva, Phys. Rev. C **69**, 014305 (2004).
[35] A. A. Raduta and D. Ionescu, Phys. Rev. C **67**, 044312 (2003).
[36] N. Minkov, S. B. Drenska, P. P. Raychev, R. P. Roussev, and D. Bonatsos, Phys. Rev. C **63**, 044305 (2001).
[37] N. Minkov, P. Yotov, S. Drenska, and W. Scheid, J. Phys. G: Nucl. Part. Phys. **32**, 497 (2006).
[38] N. V. Zamfir and D. Kusnezov, Phys. Rev. C **63**, 054306 (2001).
[39] R. Budaca, Phys. Rev. C **98**, 014303 (2018).
[40] R. Budaca, Phys. Lett. B **797**, 134853 (2019).
[41] H. Poincaré, Acta Math. **7**, 259 (1885).
[42] S. Singh and B. Singh, Nucl. Data Sheets **130**, 127 (2015).
[43] L. Gaffney *et al.*, Nature (London) **497**, 199 (2013).
[44] J. F. C. Cocks *et al.*, Nucl. Phys. A **645**, 61 (1999).
[45] H. J. Wollersheim, H. Emling, H. Grein, R. Kulessa, R. S. Simon, C. Fleischmann, J. de Boer, E. Hauber, C. Lauterbach, C. Schandera, P. A. Butler, and T. Czosnyka, Nucl. Phys. A **556**, 261 (1993).

[46] K. Abusaleem, Nucl. Data Sheets **116**, 163 (2014).
[47] P. A. Butler, L. P. Gaffney, P. Spagnoletti, K. Abrahams, M. Bowry, J. Cederkall, G. deAngelis, H. DeWitte, P. E. Garrett, A. Goldkuhle, C. Henrich, A. Illana, K. Johnston, D. T. Joss, J. M. Keatings, N. A. Kelly, M. Komorowska, J. Konki, T. Kroll, M. Lozano, B. S. NaraSingh, D. O'Donnell, J. Ojala, R. D. Page, L. G. Pedersen, C. Raison, P. Reiter, J. A. Rodriguez, D. Rosiak, S. Rothe, M. Scheck, M. Seidlitz, T. M. Shneidman, B. Siebeck, J. Sinclair, J. F. Smith, M. Stryjczyk, P. VanDuppen, S. Vinals, V. Virtanen, N. Warr, K. Wrzosek-Lipska, and M. Zielinska, Phys. Rev. Lett. **124**, 042503 (2020).
[48] Y. A. Akovali, Nucl. Data Sheets **77**, 433 (1996).
[49] E. Browne and J. K. Tuli, Nucl. Data Sheets **113**, 2113 (2012).
[50] E. Browne, Nucl. Data Sheets **107**, 2579 (2006).
[51] A. M. Demidov, L. I. Govor, V. A. Kurkin, and I. V. Mikhailov, Phys. At. Nucl. **71**, 1839 (2008).
[52] E. Browne and J. K. Tuli, Nucl. Data Sheets **108**, 681 (2007).
[53] S. S. Ntshangase, R. A. Bark, D. G. Aschman, S. Bvumbi, P. Datta, P. M. Davidson, T. S. Dinoko, M. E. A. Elbasher, K. Juhasz, E. M. A. Khaleel, A. Krasznahorkay, E. A. Lawrie, J. J. Lawrie, R. M. Lieder, S. N. T. Majola, P. L. Masiteng, H. Mohammed, S. M. Mullins, P. Nieminen, B. M. Nyako, P. Papka, D. G. Roux, J. F. Sharpey-Shafer, O. Shirinda, M. A. Stankiewicz, J. Timar, and A. N. Wilson, Phys. Rev. C **82**, 041305(R) (2010).
[54] E. Browne and J. K. Tuli, Nucl. Data Sheets **107**, 2649 (2006).
[55] E. Browne and J. K. Tuli, Nucl. Data Sheets **127**, 191 (2015).
[56] B. Birkenbach *et al.*, Phys. Rev. C **92**, 044319 (2015).
[57] B. Singh and E. Browne, Nucl. Data Sheets **109**, 2439 (2008).
[58] B. Ackermann, H. Baltzer, C. Ensel, K. Freitag, V. Grafen, C. Günther, P. Herzog, J. Manns, M. Marten-Tölle, U. Müller, J. Prinz, I. Romanski, R. Tölle, J. de Boer, N. Gollwitzer, and H. J. Maier, Nucl. Phys. A **559**, 61 (1993).
[59] F. K. McGowan, C. E. Semis, Jr., W. T. Milner, J. L. C. Ford, Jr., R. L. Robinson, and P. H. Stelson, Phys. Rev. C **10**, 1146 (1974).